

## Interfacial behavior of particle-laden bubbles under asymmetric shear flow

Eftekhari, M.; Schwarzenberger, K.; Heitkam, S.; Javadi, A.; Bashkatov, A.; Ata, S.; Eckert, K.;

Originally published:

November 2021

**Langmuir 37(2021)45, 13244-13254**

DOI: <https://doi.org/10.1021/acs.langmuir.1c01814>

Perma-Link to Publication Repository of HZDR:

<https://www.hzdr.de/publications/Publ-32831>

Release of the secondary publication  
on the basis of the German Copyright Law § 38 Section 4.

# Interfacial behavior of particle-laden bubbles under asymmetric shear flow

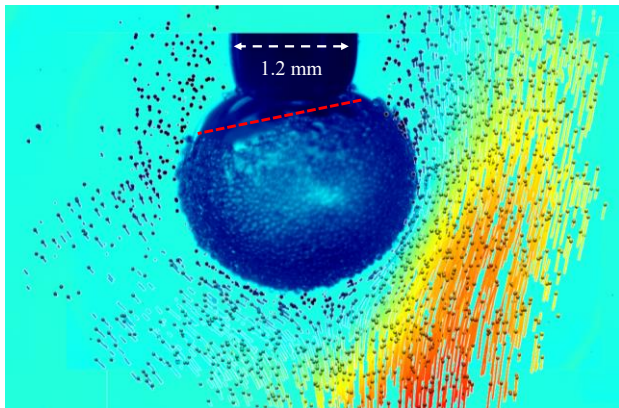
Milad Eftekhari<sup>1,2\*</sup>, Karin Schwarzenberger<sup>1,2</sup>, Sascha Heitkam<sup>1,2</sup>, Aliyar Javadi<sup>1</sup>, Aleksandr Bashkatov<sup>2</sup>, Seher Ata<sup>3</sup>, Kerstin Eckert<sup>1,2</sup>

<sup>1</sup> Institute of Fluid Dynamics, Helmholtz-Zentrum Dresden-Rossendorf, Bautzner Landstrasse 400, 01328 Dresden, Germany

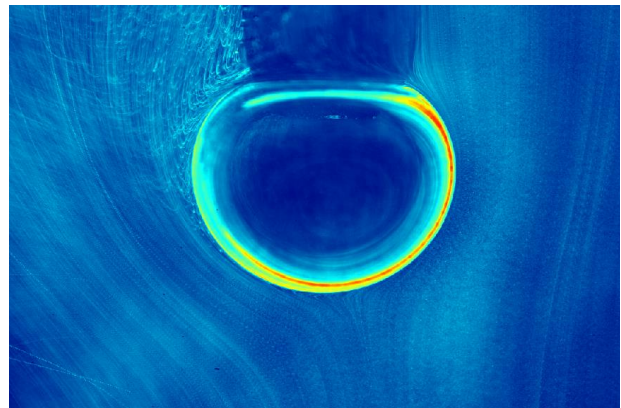
<sup>2</sup> Institute of Process Engineering and Environmental Technology, Technische Universität Dresden, 01062 Dresden, Germany

<sup>3</sup> School of Minerals and Energy Resources Engineering, University of New South Wales, Sydney, NSW, Australia

## GRAPHICAL ABSTRACT



Particle-laden bubble under asymmetric shear



Pathlines of flow for surfactant-laden bubble under asymmetric shear

## ABSTRACT

The interfacial properties of air bubbles have mostly been studied in quiescent fluids or in an axisymmetric flow field. To extend the knowledge to technologically relevant conditions, we investigate the behavior of surfactant- and particle-laden bubbles under asymmetric shear forces. Experiments are performed with a buoyant bubble at the tip of a capillary placed in a defined flow field. The response of the interface to the surrounding asymmetric flow is measured under successive reduction of the surface area. Profile analysis tensiometry is utilized to investigate the dynamic surface tension and the surface rheology of the surfactant- and particle-laden interfaces. The bulk flow and the interfacial mobility of the buoyant bubble are studied using microscopic particle image and tracking velocimetry. According to our findings, under asymmetric shear flow, surfactant-laden interfaces remain mobile regardless of the surfactant concentration. In contrast, particle-laden interfaces adopt a solid-like state and resist the interfacial flow at certain surface coverages. Elasticity measurements during successive reduction of the surface area indicate a significant change in the structure of the interface that changes its mobility. The immobilization of the interface is characterized by the ratio of the interfacial elasticity to shear forces. This dimensionless number provides an estimate the interfacial forces required to initiates interfacial immobility at defined flow field. Our findings can serve as a basis to model the boundary conditions and to modulate the hydrodynamics of bubbles and droplets with different adsorbed material.

## 1. Introduction

Surface-active materials can influence the hydrodynamic properties of multiphase systems by changing the mobility and/or deformability of the dispersed entities<sup>1-3</sup>. In the absence of surfactants, an initially spherical drop/bubble centered in an *axisymmetric flow* deforms because of the hydrodynamic forces exerted on the interface. The deformation is counteracted by the surface tension which acts to keep the drop/bubble spherical<sup>4</sup>. At low Reynolds numbers, the ratio of the viscous stress to surface tension - known as capillary number - determines the deformability of the system. However, in surfactant solutions, the fluid motion changes the distribution of surfactants at the interface, which can significantly modify the mobility and deformability of the system<sup>5-8</sup>. For example, in an *axisymmetric flow*, the fluid motion sweeps the surfactants toward the trailing edge. The resulting nonuniform distribution of the surfactants - known as stagnant cap<sup>9</sup> - creates a surface tension gradient that counteracts the viscous forces and thus reduces the mobility of the interface<sup>10-12</sup>. Since the surface tension gradient arises from the gradient of a scalar field, i.e. surface concentration, it can only counteract viscous shear stresses that are curl-free. Hence, the viscous shear stress of a *nonaxisymmetric flow* cannot be compensated by the surfactant distribution at the interface. The unbalanced stress induces a circulating flow at the interface that continuously redistributes the adsorbed surfactants and prevents the formation of a stagnant cap<sup>13</sup>. The redistribution of the surfactants also influences the shape distortion compared to a clean system<sup>14</sup>. Furthermore, it is expected to affect the hydrodynamic boundary conditions, which in turn changes the mass and heat transfer rates<sup>15</sup>.

In solutions of low molecular weight surfactants, e.g. SDS, the surfactant molecules continuously adsorb at the leading edge and desorb at the trailing edge of a moving bubble. However, the adsorption kinetic is different for larger surface-active materials such as nanoparticles (NPs). Hydrophilic NPs can form nanoparticle-surfactant complexes (NPSCs) in the presence of oppositely charged surfactants and thus become surface active<sup>16</sup>. NPs, or similarly proteins, have a substantially higher desorption energy, leading to irreversible adsorption. Hence, the formation of the dynamic adsorbed layer with adsorption at the leading edge and desorption at the trailing edge is not expected. Likewise, a different interaction between the bulk flow and interface is expected for irreversibly adsorbed materials. Here, we briefly summarize the major findings obtained for dynamic interfaces covered with different irreversibly adsorbed materials. Ybert et al.<sup>17</sup> reported the rising velocity of air bubbles with pre-adsorbed proteins and surfactants. They showed that the hydrodynamic behavior of protein-covered bubbles is similar to that of solid spheres. Additionally, they observed that the rising velocity of protein-covered bubbles in pure water remains constant whereas the surfactant-covered bubbles accelerate due to the surfactant desorption from the interface. Ulaganathan et al.<sup>18</sup> reported a stronger retardation effect in the presence of surfactants for  $\beta$ -lactoglobulin (BLG). They attributed this to the increased adsorption rate of the protein-surfactant complexes compared to the proteins. Fayazi et al.<sup>19</sup> reported an increase of drag forces in the presence of different surface-modified silica nanoparticles. Similarly, numerical studies by Yuan et al.<sup>20</sup> show that the adsorption of NPs significantly changes the boundary condition at the bubble surface, making it partially rigid. They further reported a solid body like rotation of the interface under asymmetric shear stress.

1 Despite its immediate relevance for various technological applications, a systematic  
2 experimental investigation of the hydrodynamic properties of particle-laden interfaces under  
3 asymmetric shear flow is lacking up to now. In this study, we link the hydrodynamic response of  
4 an interface with adsorbed surfactants and NPSCs to its interfacial properties. Using profile analysis  
5 tensiometry (PAT), we examine the dissimilar interfacial characteristics of NPSCs in comparison  
6 with low molecular weight surfactants. To study the behavior of particle-laden interfaces under  
7 asymmetric shear flow, a reference flow is created around a buoyant bubble placed at the tip of a  
8 capillary. Particle image/tracking velocimetry (PIV/PTV) is applied to characterize the *bulk* flow  
9 around the bubble and the *interfacial* flow on its surface. The results indicate that unlike surfactants,  
10 NPSCs can fully immobilize the interface even under asymmetric shear. This immobility implies  
11 the absence of interfacial flow and zero relative motion of adsorbed micron-sized particles on the  
12 bubble surface. We are able to quantify the immobilization of the interface by the ratio of the  
13 interfacial elasticity to the bulk viscous forces. Hence, our findings can serve as a basis to model  
14 the boundary conditions and to modulate the hydrodynamics of bubbles and droplets with different  
15 adsorbed material as present in various processes in chemical and minerals engineering.

## 16 **1. Materials and methods**

17 In general, surface-active materials can be divided into two categories based on the magnitude  
18 of their adsorption energy ( $\Delta E = \pi R_p^2 \gamma_{LV} (1 \pm \cos \theta)^2$ , see section 2.2) compared to their thermal  
19 energy (typically in the range of a few  $k_B T$ )<sup>21-23</sup>. Here,  $R_p$  is the radius of the particle,  $\gamma_{LV}$  is the  
20 surface tension,  $\theta$  is the contact angle of the particle at the interface,  $k_B$  is the Boltzmann constant,  
21 and  $T$  is the absolute temperature. The ratio of the adsorption energy to thermal energy determines  
22 the reversibility of adsorption. Particles smaller than a few nanometers have adsorption energies  
23 within the same order of magnitude as their thermal energy, while larger particles have significantly  
24 higher adsorption energies<sup>24</sup>. Consequently, the thermal energy of small surface-active molecules  
25 is sufficient to establish an adsorption-desorption equilibrium while larger surface-active materials  
26 such as polymers, proteins and particles adsorb irreversibly at the interface. Irreversibly adsorbed  
27 materials typically show a very slow dynamics of adsorption that can be accompanied by complex  
28 processes like multiple layer formation or re-orientation of the adsorbed material at the interface  
29<sup>25,26</sup>.

30 Different material classes can co-exist in practical applications. For example, in flotation,  
31 micron-sized particles correspond to the size range of the particles that can be selectively extracted.  
32 Submicron particles that are naturally present in the system can be entrained into the froth phase  
33 by the liquid film around the rising bubbles and decrease the extraction grade<sup>27</sup>. Submicron  
34 particles can also be added to the system as collectors to increase the recovery rate of the target  
35 particles<sup>28-30</sup>. Surfactants are used as collectors to hydrophobize the surface of the target particles  
36 or as frothers to control bubble size and froth stability<sup>31</sup>. To shed light on the hydrodynamics and  
37 interfacial behavior of such complex systems, we select three different particle types and two  
38 different surfactant classes:

39 (1) silica nanoparticles (NPs) as model system for submicron particles

40 (2) micron sized glass beads (GBs) in the typical size range of particles in a flotation process

- 1 (3) neutrally buoyant fluorescent polystyrene (PS) particles as tracer particles to characterize  
2 the bulk flow and track the interfacial flow
- 3 (4) a frother, the anionic surfactant sodium dodecyl benzene sulfonate (SDBS) which shows  
4 no electrostatic attraction to the negatively charged particles and is expected to adsorb  
5 mainly at the air-water interface
- 6 (5) a collector, the cationic surfactant hexadecyltrimethylammonium bromide (CTAB) which  
7 adsorbs at the surface of the negatively charged particles

8 Details on the material systems and experimental procedures are given in the following.

### 9 1.1. *Surfactants*

10 The surfactants SDBS (anionic surfactant) and CTAB (cationic surfactant) with a purity of  $\geq$   
11 99% were used as purchased (Merck, Germany). The critical micellar concentration (CMC) was  
12 found to be 2.2 mM for SDBS and 0.91 mM for CTAB, which is in good agreement with the  
13 available literature<sup>32,33</sup>.

### 14 1.2. *Particle systems and surface modification*

15 A commercially available colloidal silica nanoparticle (NP) system, Levasil 300/30 (Nouryon,  
16 Germany), was used as source dispersion. The surfactant-nanoparticle dispersion was prepared by  
17 adding 1 CMC of CTAB solution into the same volume of 0.5 wt.% nanofluid to obtain a 0.25  
18 wt.% NPs + 0.5 CMC CTAB system. The whole dispersion was continuously stirred to reduce  
19 particle aggregation<sup>33</sup>. The final sample of the surfactant-NP dispersion was sonicated in an  
20 ultrasonic bath for about 20 minutes. The temperature of the bath was controlled to avoid any  
21 destabilization or degradation within the system. Zeta potential and dynamic light scattering (DLS)  
22 measurements were performed using a NanoBrook 90Plus Zeta device (Brookhaven Instruments,  
23 USA). The experiments are carried out at 25°C including a 180 s delay after a steady device  
24 temperature has been reached to ensure the absence of temperature gradients within the sample.

25 Figure S.I.a shows the zeta potential curve measured for 0.25 wt.% silica NPs with and without  
26 CTAB. The zeta potential becomes less negative due to the adsorption of the cationic surfactant at  
27 the surface of the negatively charged silica NPs. At fixed particle concentration, the hydrophobicity  
28 of the particles is expected to increase with increasing concentration of the oppositely charged  
29 surfactant. This holds under the premise that the surfactant concentration is still too low to form a  
30 bilayer on the solid surface. Such a bilayer can establish due to hydrophobic attraction between the  
31 hydrophobic chains of the adsorbed surfactant molecules and those within the solution. The bilayer  
32 formation of cationic surfactants on the surface of a negatively charged particle reverses the surface  
33 charge of the particle and makes it hydrophilic again. Since the zeta potential remains well below  
34 zero (c.f. Figure S.I.a) bilayer formation is not expected. Therefore, it can be assumed that in the  
35 concentration range employed in this study, the surfactant addition increases the hydrophobicity of  
36 the particles.

37 Figure S.I.b plots the DLS results obtained for the dispersions employed in this study. The  
38 samples were prepared by diluting the source dispersion with deionized water to 0.25 wt.% for the  
39 DLS measurement. A certain difference in nominal diameter (9 nm) and the measured particle size  
40 (16 nm) is evident. This discrepancy can be attributed to a slight agglomeration of the particles

1 during dilution with DI water, which changes the composition and pH of the continuous phase of  
2 the original source dispersion. Figure S.I.b shows a considerable shift toward larger particle sizes  
3 with the addition of CTAB. This notable agglomeration is expected as the surface charge of the  
4 particles is neutralized by the cationic surfactant.

5 Spherical soda-lime glass beads (GBs) with a particle size between  $D_{10,3}=40.84\pm 2.58 \mu\text{m}$  and  
6  $D_{90,3}= 83.18\pm 2.20 \mu\text{m}$  (uncertainty range from three repeated laser diffraction measurements), and  
7 a specific density of  $2.5 \text{ g}\cdot\text{cm}^{-3}$  were purchased from Merck. The value  $D_{10,3}$  resp.  $D_{90,3}$  is the  
8 particle size at which 10% resp. 90% of the particle volume in the measurement range is smaller  
9 and thus characterizes the fine resp. coarse part of the size distribution. The particle size distribution  
10 of the GBs was measured using a HELOS/KR-Vario laser diffractometer (Sympatec GmbH,  
11 Germany). Figure S.II shows the cumulative size distribution of GBs employed in this study. For  
12 the zeta potential of the GBs, a value of  $-40 \text{ mV}$  at pH 9 is given in the literature<sup>34</sup>. The GBs were  
13 conditioned following Ata et al.<sup>34</sup>: two grams of GBs were added into a beaker containing 15 mL  
14 of  $1.4\times 10^{-4} \text{ mM}$  CTAB solution and stirred for about 15 min with a magnetic stirrer. The GBs have  
15 a smaller specific surface area compared to the NPs; thus, such low CTAB concentration already  
16 results in hydrophobization of the GB surface.

17 Polystyrene (PS) particles (microParticles GmbH, Germany) with a diameter of  $5.06 \mu\text{m}$ , density  
18 of  $1.02 \text{ g}\cdot\text{cm}^3$ , and an incorporated fluorescent dye (rhodamine; red fluorescent: excitation and  
19 emission at  $530 \text{ nm}$  resp.  $607 \text{ nm}$  wavelength) were used as tracer particles for the flow  
20 measurements via PIV/PTV.

### 21 1.3. Surface tension and surface deformation measurements

22 Profile analysis tensiometry (PAT-1M, Sinterface Technology, Germany) was used to evaluate  
23 the dynamic surface tension and the dilatational viscoelasticity of the air-water interface for the  
24 employed systems. Thereby, the shape profile of a pendant drop, which is determined by the  
25 interaction of gravity and surface tension, is fitted to the Young–Laplace–Gauss equation, yielding  
26 the surface tension value<sup>26</sup>. After approaching the equilibrium surface tension ( $\gamma_{eq}$ ), the elasticity  
27 modulus was measured by applying low amplitude sinusoidal perturbations to the surface area  $A$ .  
28 These regular oscillations are illustrated in Figure 1b. For such small-amplitude harmonic  
29 perturbations, the area changes can be described as

$$30 A = A_0 + \bar{A} \sin(2\pi ft) \quad (2)$$

31 where  $A_0$  is the initial surface area at equilibrium,  $\bar{A}$  is the amplitude of the area oscillations,  $f$  is  
32 the oscillation frequency, and  $t$  is the time.

33 The harmonic response of the surface tension  $\gamma$  follows as

$$34 \gamma = \gamma_{eq} + \bar{\gamma} \sin(2\pi ft + \varphi) \quad (3)$$

35 where  $\bar{\gamma}$  is the amplitude of the surface tension oscillations, and  $\varphi$  is the phase shift between the  
36 area perturbations and the surface tension response. During the imposed area oscillations, the  
37 surface tension ( $\gamma$ ) is directly acquired as a function of time. Thus, the amplitudes ( $\bar{\gamma}$ ,  $\bar{A}$ ) and the  
38 phase shift ( $\varphi$ ) can be obtained from the experimental data via Discrete Fourier Transform (DFT)  
39 algorithms. Then the complex viscoelasticity can be calculated by:

$$E(i\omega) = \frac{F[\Delta\gamma]}{F[\ln(\Delta A)]} \quad (4)$$

where  $F$  is the Fourier transform of the response relative to the perturbations. Details of the technique can be found in <sup>26,35</sup>. The oscillation amplitudes for the elasticity measurements were limited to less than 10% of the initial surface area in order to ensure mechanical equilibrium <sup>36,37</sup>. To characterize the structure of the adsorbed NPSCs and their contact angle, single cycle of large amplitude compression/expansion experiments was conducted after the elasticity measurements. The droplet surface area was gradually decreased (about 70% - 80% reduction with respect to its initial value, visible as large decrease around 5000 s in the blue curve of Figure 1a) and then increased back to the initial surface area. During this process, the change in surface tension was recorded (orange curve around 5000 s in Figure 1a). The corresponding surface pressure was evaluated as the difference between the equilibrium surface tension of the uncompressed system and the surface tension under compression ( $\Pi = \gamma_{eq} - \gamma$ ) as a function of the normalized surface area ( $A/A_0$ ) in Figure 1c. Only the compression part of the large amplitude area change was used to obtain the surface pressure curves.

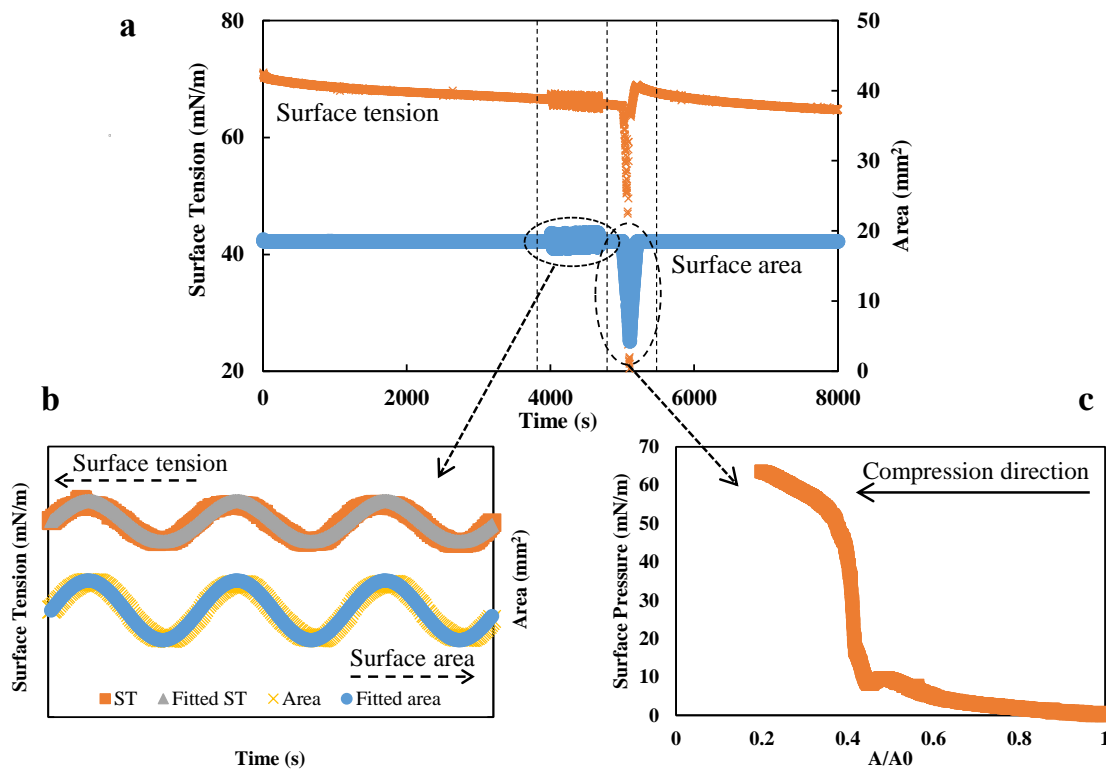


**Figure 1.** a) Protocols of surface area changes and corresponding response of surface tension, b) detail of surface area oscillations and surface tension response for measuring dilatational elasticity, and c) surface pressure evaluation during large amplitude compression.

#### 15 1.4. PIV measurements

16 The PIV measurements are conducted in a glass cuvette with a cross-sectional area of 30×30  
 17 mm<sup>2</sup> and a height of 30 mm, mounted on top of a translation stage (shown in Figure 2a). The air  
 18 bubble is formed at the tip of a straight capillary (outer diameter 1.2 mm) using a micro syringe

1 (Sinterface Technology, Germany). A steady liquid flow from the bottom to the top of the cuvette  
 2 is generated using a U-shaped nozzle of  $\sim 2$  mm inner diameter connected to a syringe pump (Ascor  
 3 med, Poland; labelled in Figure 2a). The composition of the inflowing liquid is identical to that of  
 4 the liquid in the cuvette. The relative position of the U-shaped nozzle and the bubble can be  
 5 regulated in x-direction by means of the translation stage (cf.  $\Delta x$  in Figure 2b). The resulting  
 6 asymmetric inflow induces a circulating interfacial flow on a surfactant-laden interface as observed  
 7 in Eftekhari et al.<sup>13</sup> For direct comparison, a similar horizontal displacement i.e.  $\Delta x = 1$  mm was  
 8 used in this study. The volumetric inflow rate was set to  $150 \text{ mL}\cdot\text{h}^{-1}$ , which yields an average bulk  
 9 velocity of  $\sim 13.3 \text{ mm}\cdot\text{s}^{-1}$  in the nozzle.

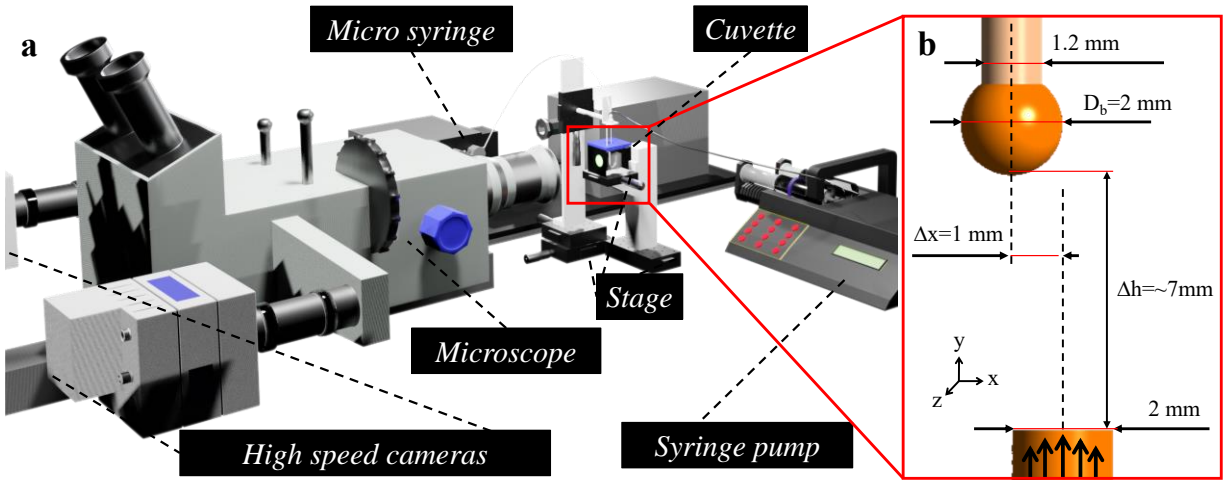


**Figure 2.** a) Stereo PIV setup to measure the velocity field. b) Definition of the geometry with a bubble at the end of a capillary placed above the flow outlet.

10 Microscopic particle image velocimetry (PIV; LaVision, Germany) was applied to characterize  
 11 the flow around the bubble and on its surface. PIV is an optical technique to measure the velocity  
 12 field in a fluid that is seeded with sufficiently small and neutrally buoyant fluorescent tracer  
 13 particles. At low Stokes numbers (cf. equation 1), the tracer particles perfectly follow the fluid flow  
 14 <sup>38</sup> and thus the fluid velocity can be assumed to be equal to the velocity of the particles. The Stokes  
 15 number is defined as:

$$16 \quad \text{St} = \frac{t_p}{t_f} = \frac{\rho_p D_p^2 U_{\text{Max}}}{18 \mu_f D_b} \quad (1)$$

17 where  $t_p$  and  $t_f$  are the relaxation time of the particle and the characteristic time scale of the flow,  
 18 respectively,  $\rho_p$  is the density of the particle,  $D_b$  and  $D_p$  are bubble and particle diameter,  
 19 respectively,  $U_{\text{Max}}$  is the maximum velocity present within the system, and  $\mu_f$  is the dynamic  
 20 viscosity of the fluid. We estimate the time scale of the flow by the fluid velocity at the inlet and  
 21 the bubble diameter as characteristic length scale of the flow. The Stokes number in our case was  
 22  $\text{St} \approx 0.01 \ll 1$ , which ensures the above-described condition of perfect advection.

23 The fluorescent particles are illuminated by a 530 nm laser and emit light with a wavelength of  
 24 607 nm (Nd-YLF laser; Photonics Industries, USA). The fluorescent signal is separated from the

1 background by an optical long-pass filter. Two high-speed cameras mounted on a stereo  
2 microscope in a slightly tilted angle record images of the measurement volume which are processed  
3 later to obtain the stereoscopic velocity field. The cameras were operated at an exposure time of  
4 100  $\mu$ s. The magnification of the imaging system was 3.2, providing a spatial resolution of 245.5  
5  $\pm$  0.4 px/mm. The thickness of the measurement volume is set by the depth of field of the optics,  
6 i.e. 0.18 mm. The parameters of the PIV system employed in this study are summarized in table 1.

7 The velocity distribution in the measurement region is calculated by correlating consecutive  
8 particle images. Details on the principle of operation can be found in Raffel et al.<sup>39</sup> Afterwards,  
9 particle tracking velocimetry (PTV) is applied as post processing to achieve higher spatial  
10 resolution (PIV evaluation software DaVis; LaVision, Germany)<sup>40</sup>. The third component of the  
11 velocity was determined by a Shake-the-Box algorithm from the stereoscopic recordings. This  
12 algorithm predicts the particle trajectory based on previous time steps and further corrects it by  
13 varying the predicted position in space (“shaking”). For a comprehensive description of this  
14 algorithm we refer to Schanz et al.<sup>41</sup>

Table 1. *Properties and parameters of the micro PIV setup.*

Image resolution	1280×800 px <sup>2</sup>
Spatial resolution	245.5±0.4 px/mm
Frame rate	200 fps
Exposure time	100 $\mu$ s
Magnification	3.2

## 15 **2. Interfacial studies**

### 16 *2.1. Surface tension and elasticity*

17 The dynamic surface tension of the aqueous system in the presence of NPs (0.25 wt.%), CTAB  
18 (0.5 CMC), and NPSCs (0.25 wt.% NPs + 0.5 CMC CTAB) is measured using PAT. Consistent  
19 with previous studies<sup>42,43</sup>, our results proved that the addition of hydrophilic silica NPs does not  
20 change the surface tension of pure water (orange triangles in Figure 3a). However, it is revealed  
21 that the addition of the same amount of NPs to a 0.5 CMC CTAB solution increases the surface  
22 tension of the surfactant solution significantly (see Figure 3a, blue squares vs. purple diamonds).  
23 This is attributed to the depletion of the surfactant molecules from the bulk solution due to the  
24 formation of complexes. During this process, the cationic molecules adsorb at the surface of the  
25 negatively charged silica NPs via electrostatic attractive forces. Consequently, the concentration of  
26 the free surfactant molecules in the solution decreases. Since the surface activity of the NPSCs is  
27 considerably lower than that of the surfactants<sup>44</sup>, the surface tension of the system increases. In  
28 other words, the NPs themselves become surface active and adsorb at the interface due to the  
29 formation of complexes. However, since their surface activity is less than that of the surfactant  
30 molecules, the surface tension of the mixture (0.25 wt.% NPs + 0.5 CMC CTAB) increases  
31 compared to the surfactant solution (0.5 CMC CTAB).

32 Figure 3b shows the dilatational elasticity of the studied systems during low amplitude  
33 sinusoidal oscillations (about 8% of the initial surface area). The elasticity values increase with  
34 increasing the oscillation frequency for both surfactant and NPSC. Due to the time scale of the

1 relaxation processes such as adsorption-desorption, re-orientation<sup>45</sup> or surface aggregation,<sup>46</sup> the  
 2 system remains further from equilibrium at higher frequencies<sup>47</sup>. The results also indicate that the  
 3 elasticity values of the solution with NPSCs are higher than that of CTAB, since it requires more  
 4 time for such large-sized compounds to respond to the surface area changes compared to the low  
 5 molecular weight surfactants.

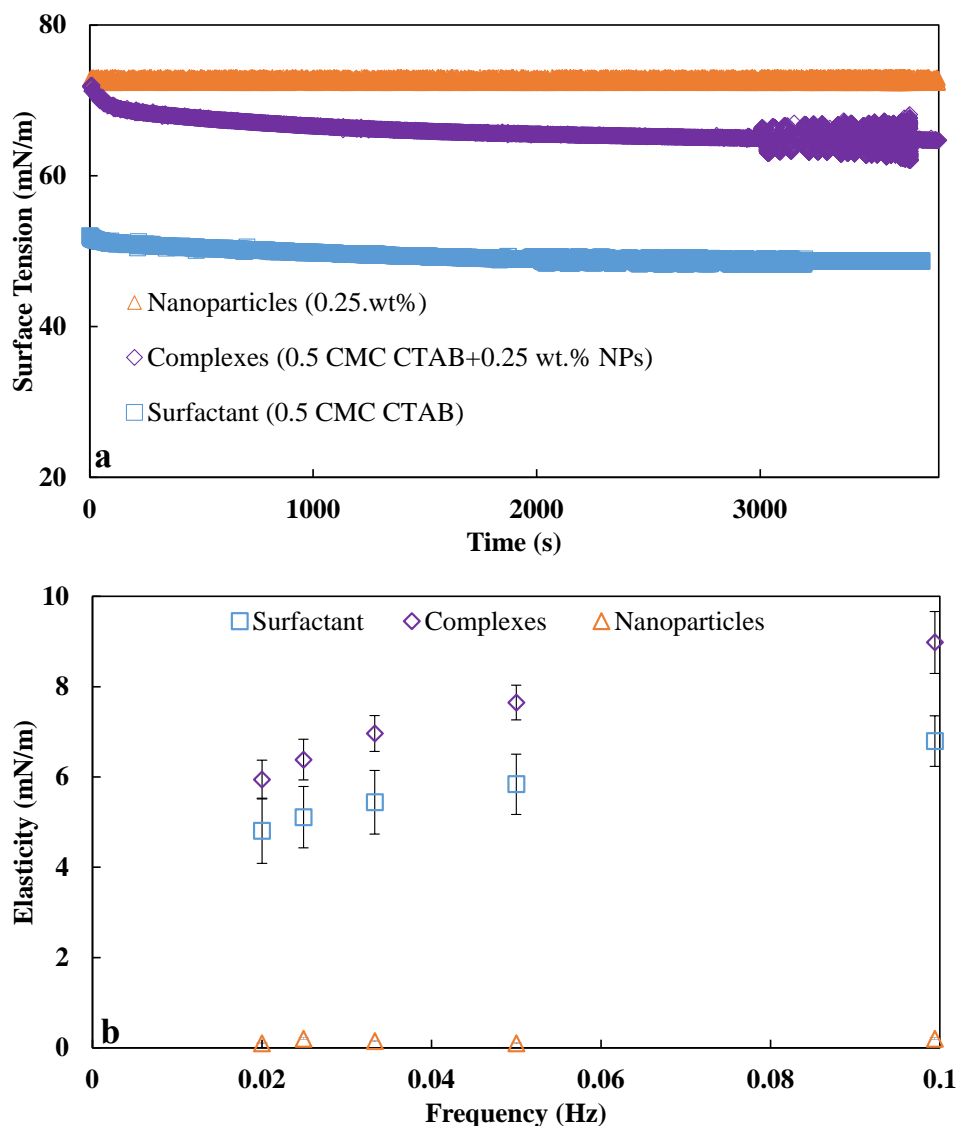


**Figure 3.** a) Dynamic surface tension measurements for 0.25 wt.% NPs, 0.5 CMC CTAB, and 0.5 CMC CTAB + 0.25 wt.% NPs; b) elasticity values of the same systems as a function of the oscillation frequency.

## 6 2.2. Large amplitude compression

7 The adsorbed layer of NPSCs was studied under large-amplitude compression of the surface area.  
 8 The graph in Figure 4 plots the surface pressure  $\Pi$  vs. normalized surface area  $A/A_0$ . The surface  
 9 pressure of the NPSC layer increases gradually with decreasing the surface area. This is related to  
 10 the irreversible adsorption of NPSCs at the interface. Upon compression, the number of complexes  
 11 per surface area and thus the surface pressure increases. However, the surface pressure rises

1 significantly sharper when the surface area decreases to less than 60% of its initial value i.e.  
 2  $A/A_0=0.6$ . The augmented concentration of the complexes at the interface increases the interparticle  
 3 interactions, which further increases the surface pressure. However, as can be seen from Figure 4,  
 4 the sharp increase of the surface pressure eventually breaks off due to the “collapse” of the  
 5 interface. The collapse of the interface is visualized in Figure 5a for a pendant aqueous drop  
 6 containing NPSCs. A solid-like skin forms on the surface of the drop upon compression. As the  
 7 compression continues pronounced wrinkles appear<sup>48</sup>. These wrinkles are less pronounced for the  
 8 fast compression of a freshly formed droplet in Figure 5b since the surface is not yet fully covered  
 9 with NPSCs. Because of the solid-like properties of the surface, the droplet shape cannot be  
 10 described anymore by the Gauss-Laplace equation so that the error in the surface tension  
 11 measurements rises with stronger surface compression. However, the characteristic shape of the  
 12 surface pressure curve can be used to estimate certain interfacial properties of the system as  
 13 described below.

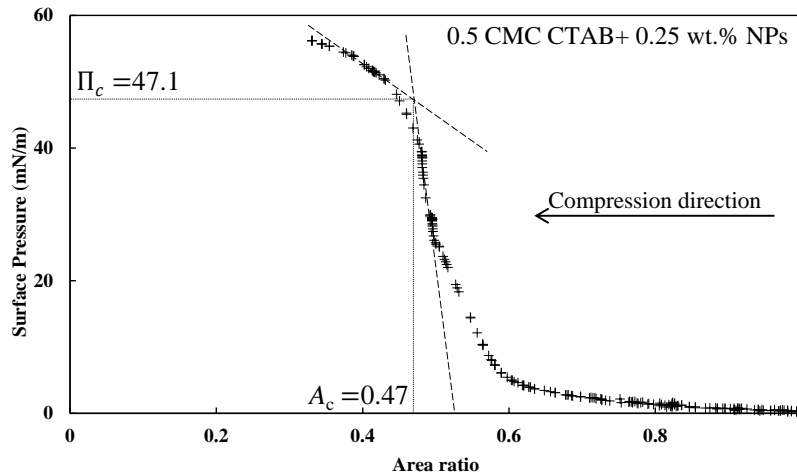


**Figure 4.** Surface pressure change during droplet surface compression for the NPSCs system. The dashed lines indicate the characteristic slopes yielding  $A_c$  and  $\Pi_c$  at their intersection for the contact angle estimation via equation (7). The solid arrow points out the temporal evolution of the compression cycle.

14 Recent studies suggest that the surface properties of the particles influence the collapse  
 15 mechanism significantly<sup>49</sup>. If the particle expulsion is the main mechanism for the interface  
 16 collapse, the particle contact angle can be determined following Clint et al.<sup>50</sup>. Note that this  
 17 assumption is drawn to allow a rough estimation of the contact angle while the actual mechanism  
 18 is not investigated within the scope of this study. For small particles, the effect of gravity is  
 19 negligible; and the energy required to remove a single particle with radius  $R_p$  from the interface  
 20 can be calculated in terms of the three-phase contact angle  $\theta$  and the interfacial energies  $\gamma$  (cf.  
 21 Figure 5d). The contact area of a particle at the interface with the aqueous phase equals  $2\pi R_p^2(1 +$   
 22  $\cos \theta)$ .

23 The water-air surface is reduced by an area of  $\pi R_p^2 \sin^2 \theta = \pi R_p^2(1 - \cos^2 \theta)$  due to the  
 24 presence of a single particle. Therefore, the energy to remove a particle from the interface is  
 25 described by:

$$1 \quad W = \pm 2\pi R_p^2 (1 \pm \cos \theta) (\gamma_{SV} - \gamma_{SL}) + \pi R_p^2 (1 - \cos^2 \theta) \gamma_{LV} \quad (5)$$

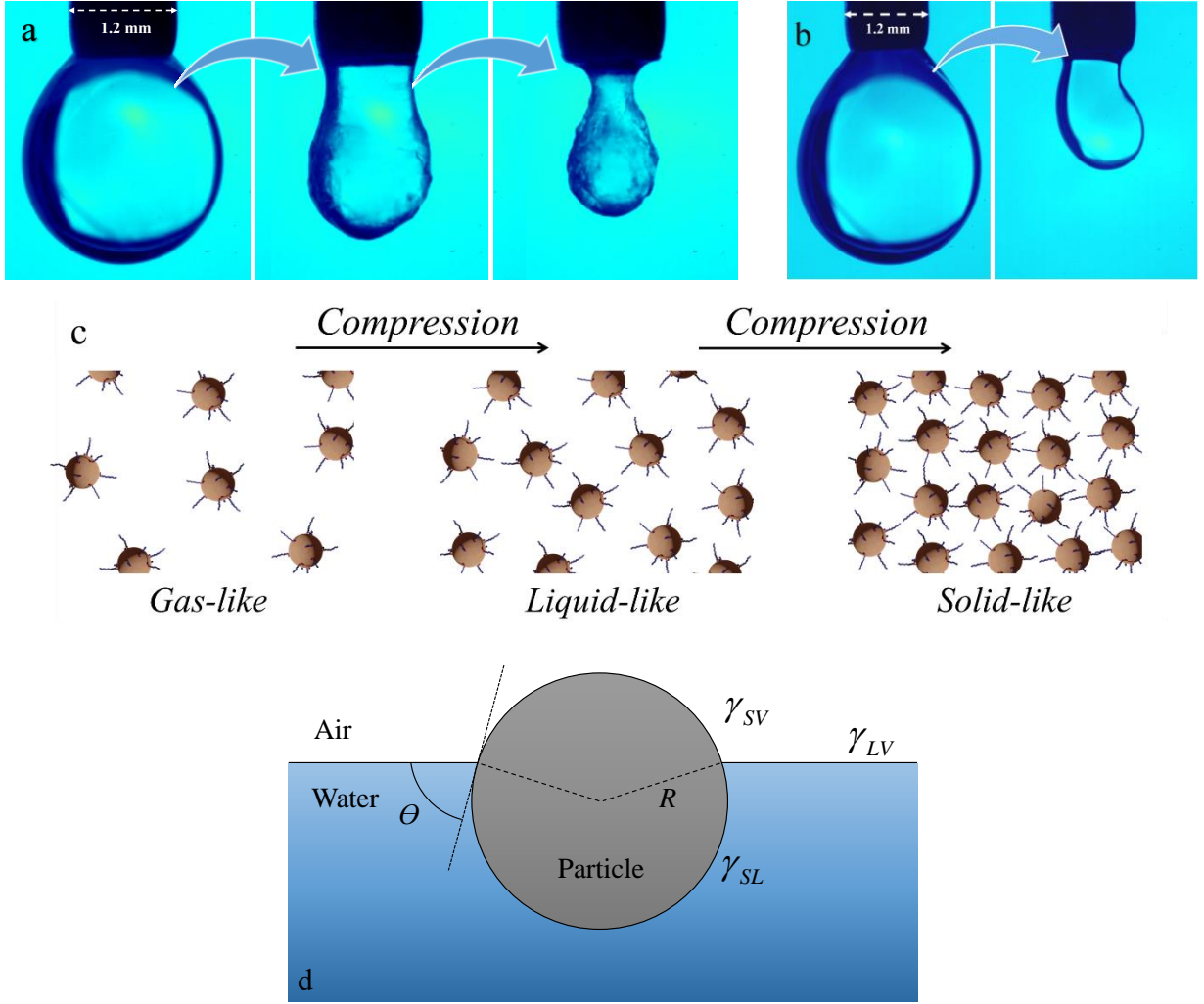


**Figure 5.** Visualization of surface solidification during large-amplitude surface compression of a drop of NPSC dispersion. Subfigure a) presents an aged drop with slow compression, while b) shows a freshly created drop during fast compression. c) Schematic of the formation of a “solid-like” skin at the water/air interface, adapted from <sup>51</sup>. d) Schematic of a particle at the interface.

2 The negative and positive signs are determined by the direction in which the particle is ejected:  
 3 negative if the particle enters the aqueous phase and positive if it enters the vapor phase. By  
 4 applying Young’s equation for the contact angle in equilibrium i.e.  $\gamma_{SV} - \gamma_{SL} = \gamma_{LV} \cos \theta$ , equation  
 5 reduces to:

$$6 \quad W = \pi R_p^2 \gamma_{LV} (1 \pm \cos \theta)^2 . \quad (6)$$

7 Again, the positive sign is for expulsion toward the vapor phase and negative for the aqueous phase.  
 8 Since the particles are waterborne and originally hydrophilic, a contact angle less than  $90^\circ$  and an  
 9 expulsion toward the water phase upon compression is assumed. Following Santini et al. <sup>52</sup> and  
 10 accounting for the number of particles at the interface, we can relate the surface pressure at the  
 11 collapse point to the contact angle:

$$12 \quad \Pi_c A_c = N_{\text{NPSCs}} \pi R_p^2 \gamma_{LV} (1 \pm \cos \theta)^2 \quad (7)$$

1 where  $N_{\text{NPSCs}}$  is the number of the NPSCs at the interface. As the inverse of the surface curvature  
 2 is expected to be much larger than the size of the NPs, the interface still can be considered as flat  
 3 at the point of collapse. The characteristic slopes of the surface pressure curve yield a critical  
 4 surface area  $A_c = 0.47$  and a critical surface pressure  $\Pi_c = 47.1$  mN/m at the kink, which defines the  
 5 interface collapse (cf. Figure 4). Using equation 7, this method estimates the contact angle of the  
 6 NPSCs to be around  $76^\circ$ .

### 7 2.3. Elasticity under stepwise surface compression

8 The elasticity values for the NPSC system were additionally measured during successive  
 9 compression of the surface area. Figure 6 shows the drop surface area, surface tension, and  
 10 determined elasticity values during the step-by-step surface compression with subsequent small-  
 11 amplitude area oscillation. The elasticity value  $E$  is observed to increase with decreasing bubble  
 12 size due to the enhanced inter-particle interactions. Additionally, a nonlinear behavior appeared in  
 13 the surface tension response, i.e. the elasticity values at higher compressions ( $E_4$  and above in  
 14 Figure 6) rise sharply. As mentioned earlier, due to the formation of a solid-like skin at the surface,  
 15 the drop adopts a non-Laplacian shape that introduces large uncertainties to the surface tension and  
 16 thus the elasticity values.

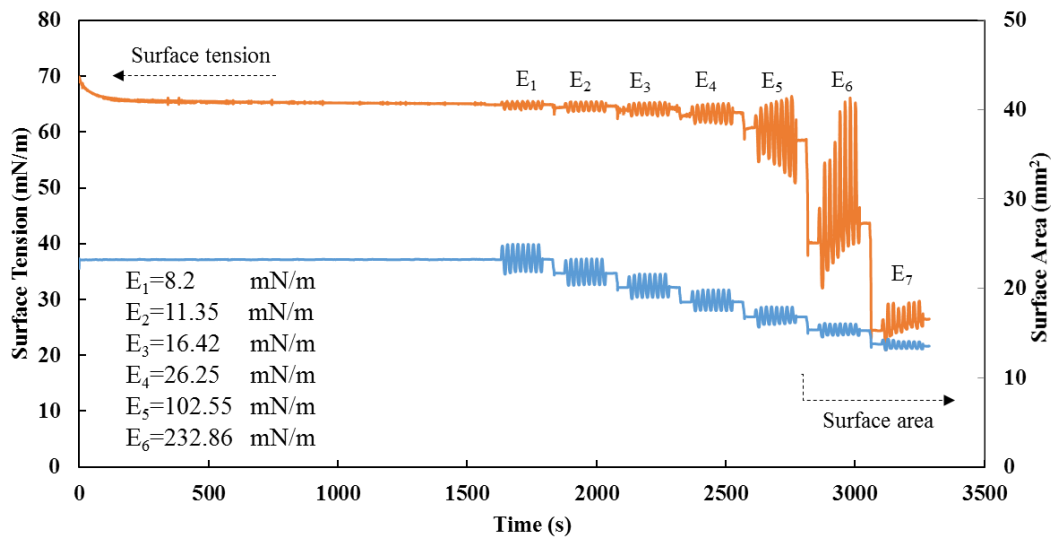


**Figure 6.** The protocol for surface area reduction and subsequent oscillation to measure the magnitude of the elasticity  $|E|$  for drops of different surface area together with corresponding surface tension curve and obtained values of  $|E|$ .

## 17 3. Hydrodynamic studies

### 18 3.1. Flow field around the bubble and on its surface

19 The flow field around the bubble was studied for the NPSC and SDBS system. After bubble  
 20 formation, a waiting time of at least 100 s was kept before the PIV measurements were started.  
 21 Together with the enhanced mass transfer due to convective mixing by the flow, this allows us to  
 22 assume that the system is close to equilibrium. Figure 7 shows the distribution of the velocity  
 23 magnitude for (a) SDBS (2.2 mM) and (b) NPSC interface under asymmetric shear flow (inflow  
 24 nozzle placed under the bubble with 1 mm horizontal shift as sketched in Figure 2b). Since the

1 concentration of SDBS is quite high, i.e. 1 CMC, a no-slip boundary condition is expected. The  
 2 low velocity values near the interface and the pronounced velocity gradients normal to the interface  
 3 for the SDBS and NPSC systems indeed suggest a no-slip boundary condition in both cases.  
 4 Additionally, it is observed that both NPSC- and SDBS-laden bubbles develop a circulating  
 5 interfacial flow under the asymmetric inflow, in response to the unbalanced viscous stress of the  
 6 bulk flow. The interfacial flow is aligned with the bulk flow on the right side and opposes the bulk  
 7 flow direction on the left side.

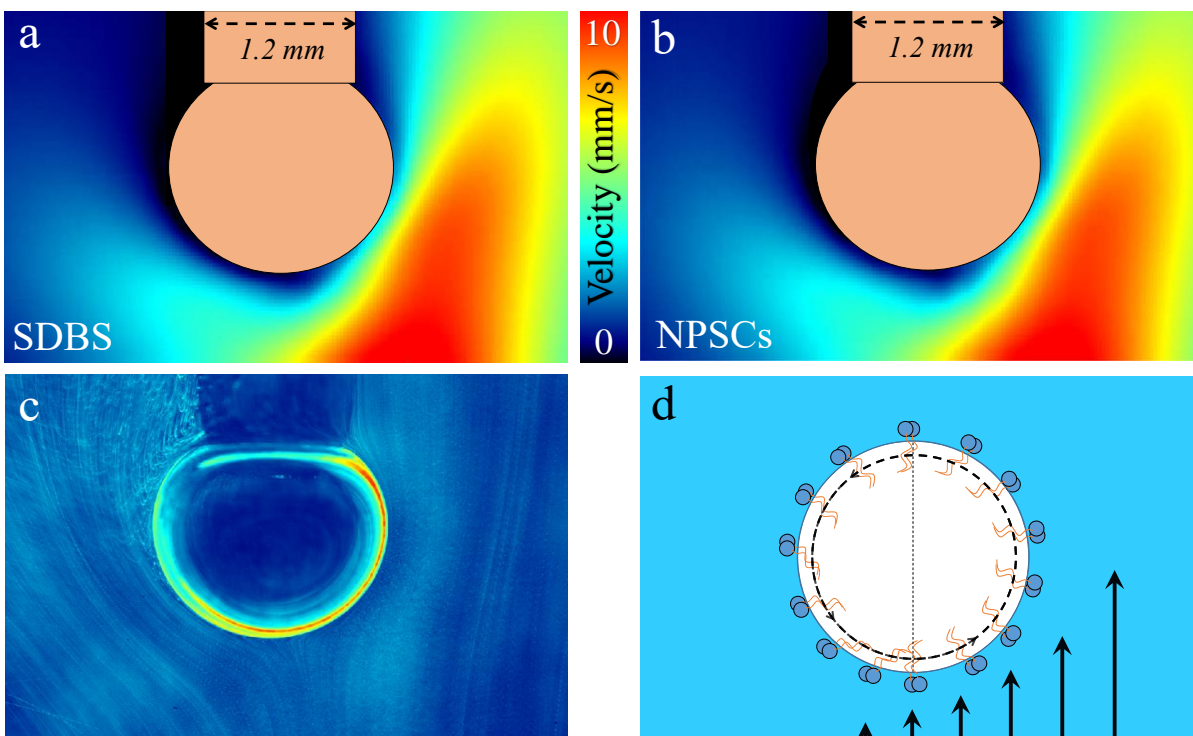


**Figure 7.** Experimental measurement of velocity distribution around a bubble attached to the tip of a capillary, given by the absolute value of the local velocity vector for a) 2.2 mM SDBS and b) NPSCs (0.25 wt.% NPs+0.5 CMC CTAB). c) Pathlines of the interfacial and bulk flow for the NPSC system; the same flow structure is observed for the SDBS system <sup>13</sup>. The color denotes the intensity of the fluorescence emitted by the particles. d) Schematic presentation of the circulating interfacial flow with adsorbed matter under shear flow.

8 Figure 7c shows the pathlines of the tracer particles both in the bulk and at interface. At the  
 9 interface the attached polystyrene tracer particles move due to the interfacial flow. The continuous  
 10 circulation indicates that a typical stagnant cap does not form because the surfactant concentration  
 11 gradient, i.e. the Marangoni stress is curl-free and thus cannot compensate the shear stress of the  
 12 surrounding asymmetric flow field. Figure 7d schematically shows the circulating surface flow that  
 13 drives and redistributes the adsorbed substances at the interface. Note that the interfacial flow  
 14 observed on the bubble surface is different from a solid body rotation, since the angular velocity is  
 15 not constant but varies spatially at the bubble surface. A more detailed study of the corresponding  
 16 bulk and interface flow field in this setup can be found in Eftekhari et al. <sup>13</sup>

17

### 1 3.2. Interfacial flow under surface compression

#### 2 3.2.1. Adsorbed nanoparticle-surfactant complexes and polystyrene tracer particles

3 In technological applications, the surface area can decrease due to processes like bubble-bubble  
4 coalescence, which can potentially increase the surface coverage. Thus, the flow measurements are  
5 repeated under successive reduction of the bubble size to understand the influence of surface area  
6 and surface coverage. The structure of the *bulk* flow field did not change considerably for both  
7 NPSC and SDBS systems under surface compression. However, the *interfacial* flow differed upon  
8 compression. While the surfactant-laden interface remained mobile throughout the whole  
9 compression, the particle-laden interfaces became immobile below a certain surface area (c.f. video  
10 V1.mp4). The switch to an immobile bubble surface implies a significant change in the structure  
11 of the interface and its fluidity. Figure 8 qualitatively plots the mobility of the bubble surface as a  
12 function of  $A/A_0$  for (a) NPSCs and (b) SDBS. In Figure 8a, the surface coverage of the bubble  
13 increases upon compression due to the irreversible adsorption of the NPSCs. This changes the  
14 nature of the interface from liquid-like to solid-like (cf. Figure 5c). In this study, only a Boolean  
15 representation (Mobility: Yes = Green; No = Red) is used to address the change of the interface  
16 state. This is because the transition from fully mobile to immobile surface occurs quite abruptly  
17 during reduction of the bubble size. A mobile surface means that there is an interfacial flow, while  
18 immobility implies the absence of measureable interfacial velocity. As plotted in Figure 8b, the  
19 surfactant-laden interface remains mobile almost throughout the entire compression cycle and the  
20 bubble surface becomes immobile only at very small sizes (video V2.mp4).

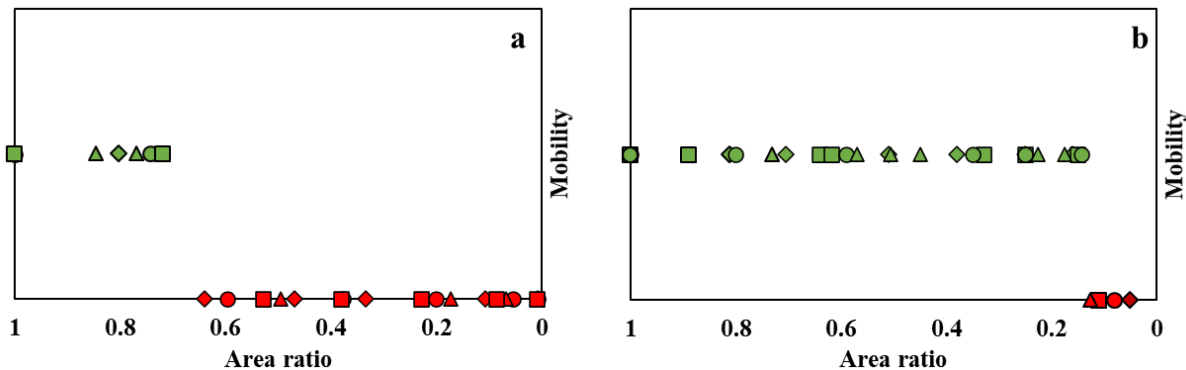


**Figure 8.** Mobility of PS tracer particles at the bubble surface as a function of the surface area ratio for (a) system with nanoparticle-surfactant complexes (NPSCs), (b) surfactant solution (SDBS). Different symbols represent different experimental runs.

21 The final immobilization is attributed to the stagnation of the flow at the solid capillary surface  
22 rather than to a change in the surface properties due to the adsorbed surfactant. In addition, at such  
23 an extremely high compression, the attached polystyrene tracer particles tend to form clusters that  
24 can adhere to the capillary and thus impede the circulating flow. The observation of a fully mobile  
25 surface over almost the entire compression range is consistent with the fact that the equilibrium  
26 surface concentration of soluble surfactants such as SDBS does not change with the surface area.  
27 It further confirms that the immobilization of the interface in the presence of NPSCs at moderate  
28 area ratios is indeed caused by the surface properties of the bubble and not by geometric size effects  
29 in the flow field.

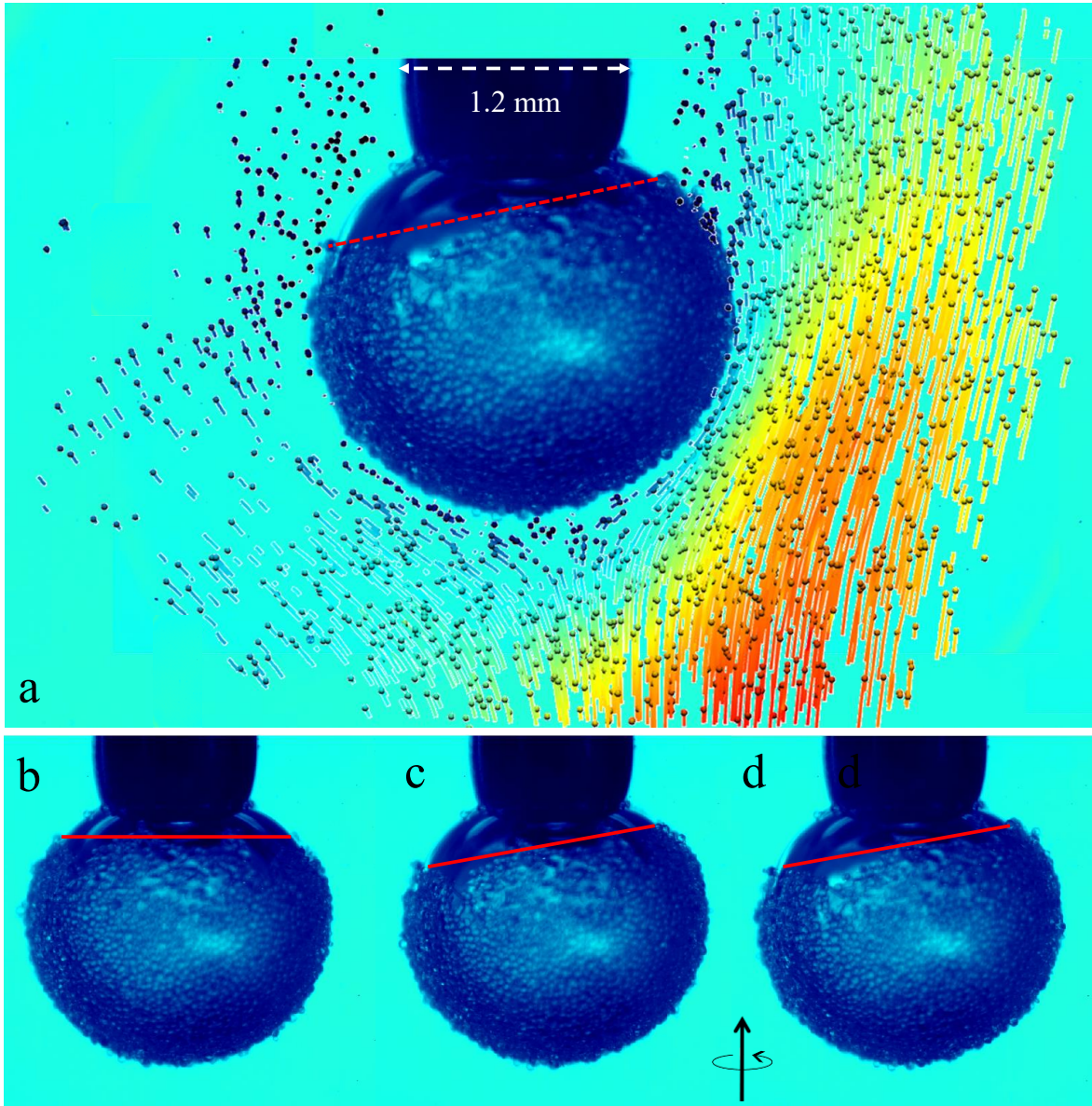


**Figure 9.** Surrounding velocity field (a) and movement of glass beads at the interface (b-d) in the absence of NPSCs. At the onset of the flow, the particle layer tilts from state (b) to (c); as the flow continues, the particle layer keeps the same tilt but rotates steadily around the vertical axis from (c) to (d).

1 3.2.2. Attached glass beads

2 In the previous sections, attached PS particles were used to track the *interfacial* flow. The  
 3 interaction of the PS particles on the bubble surface with the surrounding *bulk* flow is negligible  
 4 due to their low density difference with water and their small size. The practically relevant particles,  
 5 e.g. for flotation processes, are expected to differ from the model tracer particles. Due to their  
 6 higher densities and larger sizes, they interact significantly with the surrounding liquid. Hence,  
 7 additional flow experiments were conducted using hydrophobized glass beads instead of PS  
 8 particles. Since the glass beads (GBs) are heavier than water, they do not remain dispersed in the  
 9 quiescent aqueous phase. This prevents their spontaneous attachment to the bubble surface.

1 Therefore, to avoid sedimentation and to initiate attachment, the aqueous phase was agitated with  
2 a magnetic stirrer inside the flow cell. The number of attached GBs can be controlled by the stirring  
3 time. Before the flow measurements, the stirring was stopped and the inflow was started. For the  
4 previously used flowrate i.e.  $150 \text{ mL}\cdot\text{h}^{-1}$ , the attached GBs remained stationary at the lower apex  
5 of the bubble. Hence, to initiate movement of the GBs at the interface, the inlet flow rate had to be  
6 increased. Firstly, the flow measurements were performed in the absence of NPSCs. The behavior  
7 of a bubble fully covered with GBs under asymmetric shear flow is shown in the SI (cf. Figure  
8 S.IV). The surface properties of this fully covered bubble are similar to that of a solid sphere.  
9 However, unlike a free solid sphere in an asymmetric flow field, the coated bubble is pinned to a  
10 stationary needle. As a result, no rotation of the fully immobile interface can be induced and thus  
11 the interface and the layer of attached GBs remain stationary.

12 In the next step, the behavior of a partially covered bubble is investigated, again without added  
13 NPSCs. The snapshots in Figure 9 show that the attached GB layer forms a spherical cap. In a  
14 quiescent state, this cap is facing downwards because of gravity as displayed in Figure 9b. During  
15 inflow from the horizontally displaced nozzle, asymmetric shear stress acts on the bubble surface.  
16 A representation with 3D particle tracks is chosen in Figure 9a to enlighten the dynamics described  
17 in the following. In response to the asymmetric shear stress, the cap tilts ( $\sim 20$  degree, Figure 9b to  
18 c) and steadily rotates around its vertical axis (c to d). The rotation presumably is caused by a small  
19 out of plane component of the velocity field around the bubble. The direction of rotation can be  
20 deduced from the sign of the out of plane velocity component, cf. Figure S.III in the SI. As can be  
21 seen from this Figure,  $u_z$  is negative at the right side of the bubble driving a counterclockwise  
22 rotation of the surface when viewed from above.

### 23 3.2.3. Adsorbed nanoparticle-surfactant complexes and glass beads

24 Finally, the bubble was formed in a dispersion of NPSC and a small number of GBs (around 10-  
25 50) were attached to the bubble surface by stirring. Again, a similar shear flow was applied to the  
26 bubble surface. Under stepwise reduction of the bubble size, the mobility of the GBs was recorded  
27 at the NPSC-laden bubble surface. The evolution during the surface area compression included  
28 fully mobile (green) and immobile (red) states (see Figure 10). Additionally, an intermediate  
29 regime with partially mobile surface (marked orange in Figure 10) was observed at moderate  
30 compression. In this state, the GBs retained their mobility, but their velocity was reduced  
31 considerably. In contrast to the PS particles, the GBs interact strongly with the surrounding bulk  
32 flow because of their larger size and higher inertia\*. Hence, these particles do not directly follow  
33 the interfacial flow and a moderately compressed NPSC layer thus cannot fully arrest their motion.  
34 The limits in Figure 10 are set such that green denotes a mobile state and red an immobile state for  
35 all measurement runs. The area in between is considered as a transition from mobile to immobile.

36 As visible from the different mobility states in the orange region of Figure 10, exact  
37 reproducibility between repeated experimental runs could not be achieved at moderate  
38 compression. The discrepancies might be a consequence of a certain variation in the number of  
39 GBs attached to the bubble surface, or their relative position with respect to the inflow. The former

---

\* A certain finite size effect already is visible at few larger PS particle agglomerates moving in the opposite direction of the main interfacial flow in video V2.mp4 in the SI.

- 1 can affect the area ratio required to reach the corresponding mobility state while the latter can affect  
 2 the magnitude of the forces that the GBs experience.

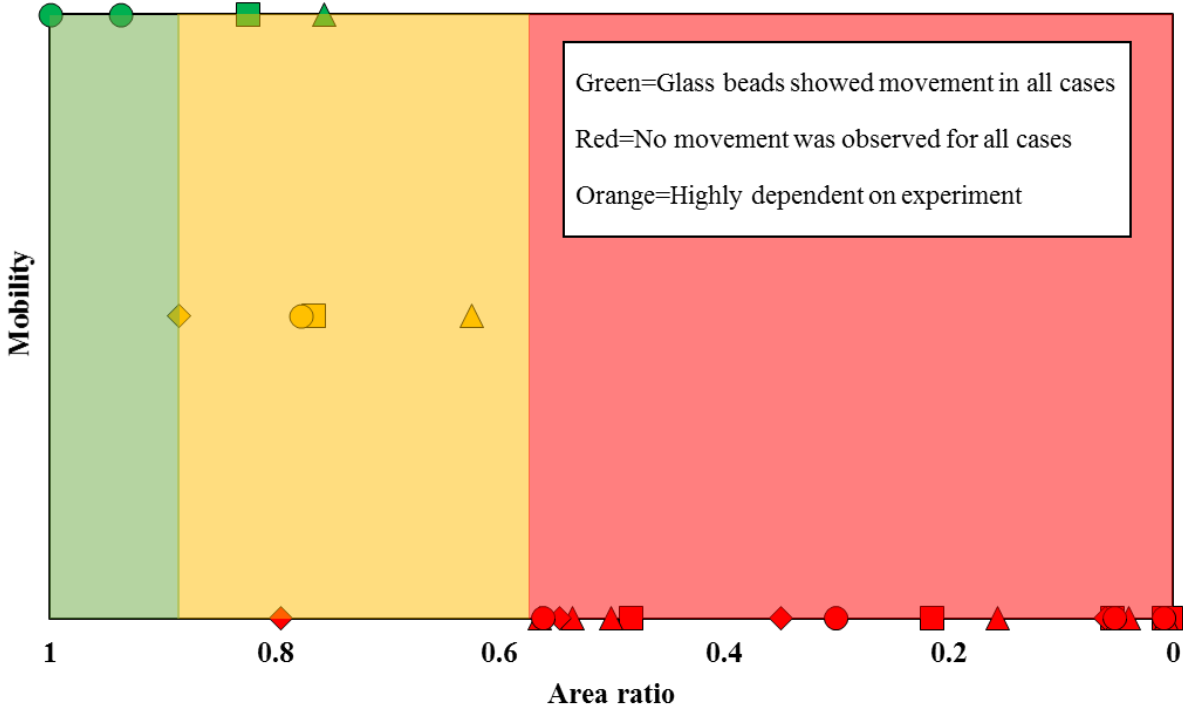


**Figure 10.** Mobility of glass beads at a bubble surface covered with NPSCs as a function of the surface area ratio. Different symbols represent different experimental runs.

- 3 The reported shift towards a solid-like state during the surface compression (c.f. Figure 5c) is in  
 4 line with the immobilization of the interface that is observed in our hydrodynamic studies with  
 5 adsorbed NPSCs. To characterize the ratio of the interfacial forces acting against the shear stress  
 6 of the flow we introduce a dimensionless number, which resembles the Marangoni number defined  
 7 by Brenner<sup>53</sup>

$$8 \quad \text{Ma}^* = E' / (F_D / R_b) \quad (8)$$

- 9 where  $E' = -d\gamma/d\ln(\Gamma)$  is the limiting value of the viscoelastic modulus for the particle-laden  
 10 interface and  $F_D / R_b$  is the drag force per unit length acting on the bubble by the asymmetric inflow.  
 11 In our experiments, the shear stress driving the interfacial flow mainly results from the different  
 12 velocity magnitudes ( $\Delta u_e$ ) on both sides of the bubble. For simplicity, we replace  $F_D$   
 13 by  $6\pi\eta_f R_b \Delta u_e$ , thus the ratio reads  $\text{Ma}^* = E' / (6\pi\eta_f \Delta u_e)$  in our configuration.

- 14 The Marangoni number defined by Brenner<sup>53</sup> describes the ratio of surface tension gradient  
 15 forces to viscous forces. However, in our case, the elasticity value expresses a rheological property  
 16 of the interface owing to the particle interactions rather than the acting surface tension gradient.  
 17 Therefore, we call this dimensionless number apparent Marangoni number ( $\text{Ma}^*$ ). The limiting  
 18 value of the elasticity ( $E'$ ) is a thermodynamic property and does not depend on the frequency of  
 19 the oscillations<sup>33</sup>. However, this quantity requires knowledge on the governing relaxation  
 20 phenomena. For our rough estimation, we simplify the problem by assuming that  $E'$  is equal to

1  $|E| = \sqrt{E'^2 + E''^2}$  at 0.05 Hz, which is the magnitude of the viscoelastic modulus at low frequency.  
 2  $|E|$  is calculated for the drops of different sizes during successive compression as depicted in Figure  
 3 6. Based on these approximate calculations (using a velocity difference of  $7.5 \text{ mm}\cdot\text{s}^{-1}$  and an  
 4 elasticity value of  $26 \text{ mN}\cdot\text{m}^{-1}$  which corresponds to the area ratio at the transition to an immobile  
 5 surface as seen in Figure 8a) a value of  $\text{Ma}^* \approx 200$  is estimated for the apparent Marangoni  
 6 number. This number provides an estimate of the critical ratio of interfacial forces to shear forces  
 7 that initiates interfacial immobility.

8 The switch to an immobile bubble surface implies a substantial change in the structure of the  
 9 interface. Since the hydrodynamic properties and the mass transfer processes in a multiphase flow  
 10 will be significantly influenced by this effect, we consider the boundary conditions at the bubble  
 11 surface in the following. For a non-deformable interface (zero normal velocity at the interface), the  
 12 shear stress balance at the interface reads

$$13 \tau^{out} - \tau^{in} = -\nabla\gamma. \quad (9)$$

14 The superscripts *in* and *out* denote the inner and outer phases. In the absence of surface tension  
 15 gradients  $\nabla\gamma$ , equation 9 reduces to  $\tau^{out} = \tau^{in}$ . Supposing that the inner phase has negligible  
 16 viscosity such as air, equation 9 further reduces to  $\tau^{out} = 0$ . This is denoted as free-slip boundary  
 17 condition and implies the absence of velocity gradients at the interface in normal direction, i.e.  
 18  $\partial u_\theta / \partial r = 0$ . Here,  $u_\theta$  is the tangential velocity component and  $r$  is the radial coordinate. In  
 19 contrast, a no-slip interface can take up shear stress from the surrounding flow i.e.  $\partial u_\theta / \partial r \neq 0$ .  
 20 Furthermore, our experiments show that under asymmetric shear stress interfacial flow exists even  
 21 at high surfactant concentration, i.e. when  $\partial u_\theta / \partial r \neq 0$ . To illustrate the above points, we  
 22 summarize the relevant boundary conditions for our bubble experiments:

- 23 • Theoretical case of ideally clean bubble: free-slip  $\partial u_\theta / \partial r = 0$  and mobile interface  $u_\theta \neq 0$
- 24 • Bubble covered with soluble surfactant: no-slip  $\partial u_\theta / \partial r \neq 0$  and mobile interface  $u_\theta \neq 0$
- 25 • Compressed, particle-laden bubble: no-slip  $\partial u_\theta / \partial r \neq 0$  and immobile interface  $u_\theta = 0$

26 Indeed, a bubble with immobile interface suspended in a liquid can show nonzero velocities at the  
 27 interface due to translation and rotation while in our setup the immobile interface is arrested by the  
 28 capillary needle. Besides, Figure S.IV in the SI indicates that a certain deformation can occur under  
 29 the dynamic pressure from the flow field. The above listed boundary conditions clearly underline  
 30 the disparate interfacial properties set by the type of adsorbed material.

### 31 **Conclusion**

32 In this work, we investigate the behavior of surfactant- and particle-laden bubbles under the  
 33 influence of asymmetric shear flow. It is revealed that the interface experiences unbalanced shear  
 34 stress that is not curl-free under asymmetric flow. These shear forces cannot be compensated by  
 35 Marangoni stress and hence provoke an interfacial flow in the presence of both surfactants and  
 36 nanoparticle-surfactant complexes (NPSCs). Although a no-slip boundary condition was observed  
 37 for both cases, the response of the interfacial flow (i.e. surface mobility) to a surface compression  
 38 (i.e. reduction of the surface area) substantially differs for each case. In the presence of soluble  
 39 surfactants, the surface concentration does not change upon compression and the interface remains  
 40 mobile. However, due to the irreversible adsorption of NPSCs, a solid-like skin may form at the

1 interface of a bubble upon compression. This skin appears when reducing the surface area below a  
2 critical fraction and immobilizes the interface. The ratio of the surface elasticity to shear force is  
3 used to describe the immobilization of the interface upon compression.

4 Our results underline that submicron particles, which are present as ultrafine fraction in many  
5 technological processes, considerably affect the interfacial and hydrodynamic properties of the  
6 system. For example, in froth flotation, the presence of adsorbed submicron particles can affect the  
7 system in two different ways. Firstly, they change the surface properties, and therefore the stability  
8 of dispersed systems or surface-driven processes like bubble-bubble coalescence<sup>54–56</sup>. Secondly,  
9 they change the hydrodynamic properties of the system, influencing flow-driven processes like  
10 bubble-particle collision or film drainage<sup>57</sup>. For the micron-sized particles which are in the typical  
11 size range of target particles in a flotation process further interaction with the surrounding flow  
12 field by their geometrical extension and density effects have to be considered.

13 To conclude with a practical example, we consider the coalescence of three bubbles with equal  
14 size. The surface area of the combined bubble equals 69% of the initial surface area, which  
15 according to our findings can cause a mobile surface to become immobile in the presence of  
16 adsorbed fine particles. In order to gain an in depth understanding of the mechanisms causing the  
17 immobilization, future studies should include a defined variation of nanoparticle size, concentration  
18 and hydrophobicity. Coupled with measurements of the interfacial velocity field under surface  
19 compression in very fine steps this may provide further insights on the processes during the abrupt  
20 transition to an immobile interface.

## 21 **Acknowledgement**

22 The authors would like to thank Nouryon (formerly AkzoNobel Specialty Chemicals) for  
23 supplying the nanoparticle dispersions. Funding by the European Union's Horizon 2020 research  
24 and innovation program under grant agreement No 821265 is gratefully acknowledged.  
25 Furthermore, we acknowledge the financial support provided by the German Helmholtz  
26 Association.

## 27 **Supplementary material**

28 Electronic supplementary information (ESI) available. In the supplementary material, the size  
29 distribution of nanoparticles (NPs) and glass bead (GBs) along with zeta potential measurements  
30 of the employed NPs are reported. Furthermore, the out of plane velocity component for Figure 9  
31 and the response of a bubble fully covered with GBs to the asymmetric flow are shown. Two videos  
32 visualize the mobility of the interface under successive compression for complex- and surfactant-  
33 laden interfaces.

## 34 **References**

- 35 (1) Tzounakos, A.; Karamanev, D. G.; Margaritis, A.; Bergougnou, M. A. Effect of the  
36 Surfactant Concentration on the Rise of Gas Bubbles in Power-Law Non-Newtonian  
37 Liquids. *Ind. Eng. Chem. Res.* **2004**, *43* (18), 5790–5795.
- 38 (2) Pawliszak, P.; Ulaganathan, V.; Bradshaw-Hajek, B. H.; Manica, R.; Beattie, D. A.;  
39 Krasowska, M. Mobile or Immobile? Rise Velocity of Air Bubbles in High-Purity Water.  
40 *J. Phys. Chem. C* **2019**, *123* (24), 15131–15138.

- 1 (3) Nock, W. J.; Heaven, S.; Banks, C. J. Mass Transfer and Gas-Liquid Interface Properties  
2 of Single CO<sub>2</sub> Bubbles Rising in Tap Water. *Chem. Eng. Sci.* **2016**, *140*, 171–178.
- 3 (4) Stone, H. A. Dynamics of Drop Deformation and Breakup in Viscous Fluids. *Annu. Rev.*  
4 *Fluid Mech.* **1994**, *26* (1), 65–102.
- 5 (5) Panigrahi, D. P.; Das, S.; Chakraborty, S. Deformation of a Surfactant-Laden Viscoelastic  
6 Droplet in a Uniaxial Extensional Flow. *Phys. Fluids* **2018**, *30* (12).
- 7 (6) Das, S.; Manda, S.; Chakraborty, S. Cross-Stream Migration of a Surfactant-Laden  
8 Deformable Droplet in a Poiseuille Flow. *Phys. Fluids* **2017**, *29* (8).
- 9 (7) Mandal, S.; Ghosh, U.; Chakraborty, S. Effect of Surfactant on Motion and Deformation of  
10 Compound Droplets in Arbitrary Unbounded Stokes Flows. *J. Fluid Mech.* **2016**, *803*,  
11 200–249.
- 12 (8) Bazhlekov, I. B.; Anderson, P. D.; Meijer, H. E. H. Numerical Investigation of the Effect  
13 of Insoluble Surfactants on Drop Deformation and Breakup in Simple Shear Flow. *J.*  
14 *Colloid Interface Sci.* **2006**, *298* (1), 369–394.
- 15 (9) Fleckenstein, S.; Bothe, D. Simplified Modeling of the Influence of Surfactants on the Rise  
16 of Bubbles in VOF-Simulations. *Chem. Eng. Sci.* **2013**, *102*, 514–523.
- 17 (10) Dukhin, S. S.; Lotfi, M.; Kovalchuk, V. I.; Bastani, D.; Miller, R. Dynamics of Rear  
18 Stagnant Cap Formation at the Surface of Rising Bubbles in Surfactant Solutions at Large  
19 Reynolds and Marangoni Numbers and for Slow Sorption Kinetics. *Colloids Surfaces A*  
20 *Physicochem. Eng. Asp.* **2016**, *492*, 127–137.
- 21 (11) Ramírez-Muñoz, J.; Galicia-Nequiz, O. G.; Baz-Rodríguez, S.; Colín-Luna, J. A.;  
22 Martínez-Delgado, S. A.; Puebla, H. The Effects of Surfactants on the Drag of a Bubble.  
23 *Procedia Eng.* **2012**, *42*, 1840–1848.
- 24 (12) Dukhin, S. S.; Kovalchuk, V. I.; Gochev, G. G.; Lotfi, M.; Krzan, M.; Malysa, K.; Miller,  
25 R. Dynamics of Rear Stagnant Cap Formation at the Surface of Spherical Bubbles Rising  
26 in Surfactant Solutions at Large Reynolds Numbers under Conditions of Small Marangoni  
27 Number and Slow Sorption Kinetics. *Adv. Colloid Interface Sci.* **2015**, *222*, 260–274.
- 28 (13) Eftekhari, M.; Schwarzenberger, K.; Heitkam, S.; Eckert, K. Interfacial Flow of a  
29 Surfactant-Laden Interface under Asymmetric Shear Flow. *J. Colloid Interface Sci.* **2021**,  
30 *599*, 837–848.
- 31 (14) Vlahovska, P. M.; Bławdziewicz, J.; Loewenberg, M. Small-Deformation Theory for a  
32 Surfactant-Covered Drop in Linear Flows. *J. Fluid Mech.* **2009**, *624*, 293–337.
- 33 (15) Frey, D. D.; King, C. J. Effects of Surfactants on Mass Transfer during Spray Drying.  
34 *AIChE J.* **1986**, *32* (3), 437–443.
- 35 (16) Zhou, Y.; Wu, X.; Zhong, X.; Sun, W.; Pu, H.; Zhao, J. X. Surfactant-Augmented  
36 Functional Silica Nanoparticle Based Nanofluid for Enhanced Oil Recovery at High  
37 Temperature and Salinity. *ACS Appl. Mater. Interfaces* **2019**, *11* (49), 45763–45775.
- 38 (17) Ybert, C.; Di Meglio, J. M. Ascending Air Bubbles in Protein Solutions. *Eur. Phys. J. B*  
39 **1998**, *4* (3), 313–319.

- 1 (18) Ulaganathan, V.; Krzan, M.; Lotfi, M.; Dukhin, S. S.; Kovalchuk, V. I.; Javadi, A.; Gunes,  
2 D. Z.; Gehin-Delval, C.; Malysa, K.; Miller, R. Influence of  $\beta$ -Lactoglobulin and Its  
3 Surfactant Mixtures on Velocity of the Rising Bubbles. *Colloids Surfaces A Physicochem.*  
4 *Eng. Asp.* **2014**, *460*, 361–368.
- 5 (19) Fayzi, P.; Bastani, D.; Lotfi, M.; Miller, R. Influence of Surface-Modified Nanoparticles  
6 on the Hydrodynamics of Rising Bubbles. *Chem. Eng. Technol.* **2021**, *44* (3), 513–520.
- 7 (20) Yuan, Y.; Li, X.; Tu, J. The Effects of Nanoparticles on the Lift Force and Drag Force on  
8 Bubbles in Nanofluids: A Two-Fluid Model Study. *Int. J. Therm. Sci.* **2017**, *119*, 1–8.
- 9 (21) Böker, A.; He, J.; Emrick, T.; Russell, T. P. Self-Assembly of Nanoparticles at Interfaces.  
10 *Soft Matter* **2007**, *3* (10), 1231–1248.
- 11 (22) Lin, Y.; Böker, A.; Skaff, H.; Cookson, D.; Dinsmore, A. D.; Emrick, T.; Russell, T. P.  
12 Nanoparticle Assembly at Fluid Interfaces: Structure and Dynamics. *Langmuir* **2005**, *21*  
13 (1), 191–194.
- 14 (23) Lin, Y.; Skaff, H.; Emrick, T.; Dinsmore, A. D.; Russell, T. P. Nanoparticle Assembly and  
15 Transport at Liquid-Liquid Interfaces. *Science* **2003**, *299* (5604), 226–229.
- 16 (24) Zeng, C.; Bissig, H.; Dinsmore, A. D. Particles on Droplets: From Fundamental Physics to  
17 Novel Materials. *Solid State Commun.* **2006**, *139* (11–12), 547–556.
- 18 (25) Pan, F.; Lu, Z.; Tucker, I.; Hosking, S.; Petkov, J.; Lu, J. R. Surface Active Complexes  
19 Formed between Keratin Polypeptides and Ionic Surfactants. *J. Colloid Interface Sci.*  
20 **2016**, *484*, 125–134.
- 21 (26) Loglio, G.; Pandolfini, P.; Makievski, A. V.; Ravera, F.; Ferrari, M.; Liggieri, L. Novel  
22 Methods to Study Interfacial Layers. *Stud. Interface Sci.* **2001**, *11*, 439–483.
- 23 (27) Schubert, H. On the Optimization of Hydrodynamics in Fine Particle Flotation. *Miner.*  
24 *Eng.* **2008**, *21* (12–14), 930–936.
- 25 (28) Yang, S.; Pelton, R.; Raegen, A.; Montgomery, M.; Dalnoki-Veress, K. Nanoparticle  
26 Flotation Collectors: Mechanisms behind a New Technology. *Langmuir* **2011**, *27* (17),  
27 10438–10446.
- 28 (29) Yang, S.; Razavizadeh, B. B. M.; Pelton, R.; Bruin, G. Nanoparticle Flotation Collectors -  
29 The Influence of Particle Softness. *ACS Appl. Mater. Interfaces* **2013**, *5* (11), 4836–4842.
- 30 (30) Yang, S.; Pelton, R.; Montgomery, M.; Cui, Y. Nanoparticle Flotation Collectors III: The  
31 Role of Nanoparticle Diameter. *ACS Appl. Mater. Interfaces* **2012**, *4* (9), 4882–4890.
- 32 (31) Liu, D.; Somasundaran, P. Role of Collector and Frother, and of  
33 Hydrophobicity/Oleophilicity of Pyrite on the Separation of Pyrite from Coal by Flotation.  
34 *Int. J. Miner. Process.* **1994**, *41* (3–4), 227–238.
- 35 (32) Zamora, J. M.; Marquez, R.; Forgiarini, A. M.; Langevin, D.; Salager, J. L. Interfacial  
36 Rheology of Low Interfacial Tension Systems Using a New Oscillating Spinning Drop  
37 Method. *J. Colloid Interface Sci.* **2018**, *519*, 27–37.
- 38 (33) Liggieri, L.; Santini, E.; Guzmán, E.; Maestro, A.; Ravera, F. Wide-Frequency Dilational  
39 Rheology Investigation of Mixed Silica Nanoparticle-CTAB Interfacial Layers. *Soft*

- 1        *Matter* **2011**, 7 (17), 7699–7709.
- 2 (34) Ata, S. Coalescence of Bubbles Covered by Particles. *Langmuir* **2008**, 24 (7), 6085–6091.
- 3 (35) Ravera, F.; Loglio, G.; Kovalchuk, V. I. Interfacial Dilational Rheology by Oscillating  
4 Bubble/Drop Methods. *Curr. Opin. Colloid Interface Sci.* **2010**, 15 (4), 217–228.
- 5 (36) Leser, M. E.; Acquistapace, S.; Cagna, A.; Makievski, A. V.; Miller, R. Limits of  
6 Oscillation Frequencies in Drop and Bubble Shape Tensiometry. In *Colloids and Surfaces*  
7 *A: Physicochemical and Engineering Aspects*; 2005; Vol. 261, pp 25–28.
- 8 (37) Ravera, F.; Ferrari, M.; Santini, E.; Liggieri, L. Influence of Surface Processes on the  
9 Dilational Visco-Elasticity of Surfactant Solutions. *Adv. Colloid Interface Sci.* **2005**, 117  
10 (1–3), 75–100.
- 11 (38) Lau, T. C. W.; Nathan, G. J. The Effect of Stokes Number on Particle Velocity and  
12 Concentration Distributions in a Well-Characterised, Turbulent, Co-Flowing Two-Phase  
13 Jet. *J. Fluid Mech.* **2016**, 809, 72–110.
- 14 (39) Raffel, M.; Willert, C. E.; wereley, steven; Kompenhans, J. *Particle Image Velocimetry: A*  
15 *Practical Guide*; Engineering online library; Springer Berlin Heidelberg, 2001.
- 16 (40) Schneiders, J. F. G.; Scarano, F.; Elsinga, G. E. Resolving Vorticity and Dissipation in a  
17 Turbulent Boundary Layer by Tomographic PTV and VIC+. *Exp. Fluids* **2017**, 58 (4), 1–  
18 14.
- 19 (41) Schanz, D.; Gesemann, S.; Schröder, A. Shake-The-Box: Lagrangian Particle Tracking at  
20 High Particle Image Densities. *Exp. Fluids* **2016**, 57 (5), 1–27.
- 21 (42) Matter, S.; Maestro, A.; Guzm, E.; Santini, E.; Ravera, F.; Liggieri, L.; Ortega, F.  
22 Wettability of Silica Nanoparticle – Surfactant Nanocomposite Interfacial Layers. **2012**,  
23 837–843.
- 24 (43) Eftekhari, M.; Schwarzenberger, K.; Javadi, A.; Eckert, K. The Influence of Negatively  
25 Charged Silica Nanoparticles on the Surface Properties of Anionic Surfactants:  
26 Electrostatic Repulsion or the Effect of Ionic Strength? *Phys. Chem. Chem. Phys.* **2020**, 22  
27 (4), 2238–2248.
- 28 (44) Ravera, F.; Santini, E.; Loglio, G.; Ferrari, M.; Liggieri, L. Effect of Nanoparticles on the  
29 Interfacial Properties of Liquid/Liquid and Liquid/Air Surface Layers. *J. Phys. Chem. B*  
30 **2006**, 110 (39), 19543–19551.
- 31 (45) Ravera, F.; Ferrari, M.; Miller, R.; Liggieri, L. Dynamic Elasticity of Adsorption Layers in  
32 the Presence of Internal Reorientation Processes. *J. Phys. Chem. B* **2001**, 105 (1), 195–203.
- 33 (46) Palazzolo, R.; Ravera, F.; Ferrari, M.; Liggieri, L. Dynamic Surface Elasticity of  
34 Adsorption Layers in the Presence of a Surface Phase Transition from Monomers to Large  
35 Aggregates. *Langmuir* **2002**, 18 (9), 3592–3599.
- 36 (47) Ravera, F.; Ferrari, M.; Liggieri, L.; Loglio, G.; Santini, E.; Zanobini, A. Liquid-Liquid  
37 Interfacial Properties of Mixed Nanoparticle-Surfactant Systems. *Colloids Surfaces A*  
38 *Physicochem. Eng. Asp.* **2008**, 323 (1–3), 99–108.
- 39 (48) Asekomhe, S. O.; Chiang, R.; Masliyah, J. H.; Elliott, J. A. W. Some Observations on the

- 1 Contraction Behavior of a Water-in-Oil Drop with Attached Solids. *Ind. Eng. Chem. Res.*  
2 **2005**, *44* (5), 1241–1249.
- 3 (49) Razavi, S.; Cao, K. D.; Lin, B.; Lee, K. Y. C.; Tu, R. S.; Kretzschmar, I. Collapse of  
4 Particle-Laden Interfaces under Compression: Buckling vs Particle Expulsion. *Langmuir*  
5 **2015**, *31* (28), 7764–7775.
- 6 (50) Clint, J. H.; Taylor, S. E. Particle Size and Interparticle Forces of Overbased Detergents: A  
7 Langmuir Trough Study. *Colloids and Surfaces* **1992**, *65* (1), 61–67.
- 8 (51) Chai, Y.; Lukito, A.; Jiang, Y.; Ashby, P. D.; Russell, T. P. Fine-Tuning Nanoparticle  
9 Packing at Water-Oil Interfaces Using Ionic Strength. *Nano Lett.* **2017**, *17* (10), 6453–  
10 6457.
- 11 (52) Santini, E.; Ravera, F.; Miller, R.; Liggieri, L.; Krägel, J. Study of the Monolayer Structure  
12 and Wettability Properties of Silica Nanoparticles and CTAB Using the Langmuir Trough  
13 Technique. *Colloids Surfaces A Physicochem. Eng. Asp.* **2010**, *382* (1–3), 186–191.
- 14 (53) Brenner, H. *Interfacial Transport Processes and Rheology*; Elsevier, 2013.
- 15 (54) Cho, Y. S.; Laskowski, J. S. Effect of Flotation Frothers on Bubble Size and Foam  
16 Stability. *Int. J. Miner. Process.* **2002**, *64* (2–3), 69–80.
- 17 (55) Lucassen-Reynders, E. H.; Wasan, D. T. Interfacial Viscoelasticity in Emulsions and  
18 Foams. *Food. Struct.* **1993**, *12* (1), 1–12.
- 19 (56) Hunter, T. N.; Pugh, R. J.; Franks, G. V.; Jameson, G. J. The Role of Particles in  
20 Stabilising Foams and Emulsions. *Adv. Colloid Interface Sci.* **2008**, *137* (2), 57–81.
- 21 (57) Xing, Y.; Gui, X.; Pan, L.; Pinchasik, B. El; Cao, Y.; Liu, J.; Kappl, M.; Butt, H. J. Recent  
22 Experimental Advances for Understanding Bubble-Particle Attachment in Flotation. *Adv.*  
23 *Colloid Interface Sci.* **2017**, *246* (May), 105–132.
- 24